International Journal of Hydrogen Energy 270 (2026) 157103

Contents lists available at ScienceDirect

International Journal of Hydrogen Energy

journal homepage: www.elsevier.com/locate/he

The effect of end-gas auto-ignition flame properties on the knocking intensity of a dual-fuel hydrogen engine

Riku Okamoto [a], Nobuyuki Kawahara [b,*], Yoshimitsu Kobashi [b]

[a] Graduate School of Environmental, Life, Natural Science and Technology, Okayama University, 3-1-1, Tsushima-Naka, Okayama, 700-8530, Japan
[b] Faculty of Environmental, Life, Natural Science and Technology, Okayama University, 3-1-1, Tsushima-Naka, Okayama, 700-8530, Japan

ARTICLE INFO

Keywords:
Dual-fuel engine
Hydrogen
End-gas auto-ignition
Knocking intensity
Visualization

ABSTRACT

This study sought to elucidate the mechanism governing PRE-mixed mixture ignition in end-gas region (PREMIER) combustion in a dual-fuel hydrogen engine. Both knocking and PREMIER combustion are induced by end-gas auto-ignition, but differ in terms of the subsequent development of pressure waves. Knocking is accompanied by strong waves, whereas PREMIER combustion is characterized by the absence of, or very few, such waves. End-gas auto-ignition of hydrogen–air mixtures was visualized while in-cylinder pressure was measured using an optical compression and expansion machine. The visualization data indicate that KI increased as the spread velocity of the end-gas auto-ignition front rose. That velocity remained below 100 m/s during PREMIER combustion, but attained approximately 400 m/s in severe knocking cycles. The theory proposed by Bradley was used to evaluate the experimental results, and two dimensionless parameters, ξ and ε, were estimated. The ξ-ε diagram showed a distinct transition from PREMIER combustion to knocking. (150 words).

1. Introduction

The high-efficiency operation of hydrogen-fueled internal combustion engines has attracted considerable attention as a means of mitigating global warming. As hydrogen contains no carbon, combustion produces no CO_2, a major greenhouse gas. Furthermore, hydrogen can be produced via water electrolysis using electricity generated from renewable energy sources [1]. Therefore, use of hydrogen as fuel may enable efficient energization of an entire system with minimal environmental impact. When hydrogen powers an internal combustion engine, an external ignition source is generally required because hydrogen exhibits a higher auto-ignition temperature than those of compressed natural gas and gasoline, rendering compression ignition difficult under typical operating conditions [2]. Various platforms have been developed to achieve efficient hydrogen combustion, including spark-ignited direct-injection, pre-chamber spark-ignited, spark-ignited rotary [3,4] and diesel-ignited dual-fuel engines. This study focused on dual-fuel engines because dual-fuel combustion has emerged as a promising approach for effective heavy-duty and marine applications. When gaseous and pilot fuels are combined in such engines, both stable ignition and compliance with stringent emission regulations are possible [5]. Previous studies demonstrated that hydrogen-fueled dual-fuel operation could achieve a brake thermal efficiency comparable to that of conventional diesel engines operating under certain conditions [6–9]. Furthermore, from a practical perspective, a dual-fuel combustion system can be implemented in existing diesel engines with relatively minor modifications. It can also be operated using only diesel fuel depending on the situation [10]. For these reasons, the dual-fuel engine is considered a promising platform for the hydrogen utilization and was therefore selected as the subject of the present study. The carbon-free nature of hydrogen aside, the gas exhibits unique physicochemical properties, including a wide flammability range and a high burning velocity that enable lean combustion and shorten the combustion duration compared to those of conventional fuels [2]. Such characteristics improve engine performance. However, the distinct characteristics of hydrogen are associated with abnormal combustion phenomena, including pre-ignition, backfire, and knocking. In particular, the latter remains a major challenge when designing hydrogen engines with high compression ratios or that operate under high loads [5].

Knocking is caused by end-gas auto-ignition at a hot spot where the local temperature or radical concentration is higher than that of the surrounding mixture. The end-gas is compressed by both piston motion and flame propagation, triggering auto-ignition onset. The associated, rapid energy release generates pressure waves in the combustion

* Corresponding author.
E-mail address: kawahara@okayama-u.ac.jp (N. Kawahara).

https://doi.org/10.1016/j.ijhydene.2026.157103
Received 14 June 2026; Received in revised form 6 August 2026; Accepted 14 August 2026
Available online 24 August 2026

chamber, associated with pressure oscillations, audible noise, and (possibly) serious engine damage [11]. As knocking constrains both the engine operating conditions and the compression ratios, a thorough understanding of knocking is essential. To this end, experiments using optically accessible engines [12–21] and numerical simulations [22–24] have offered crucial insights into knocking phenomena. In addition to studies on conventional knocking, hydrogen knocking has attracted considerable research attention in recent years because hydrogen possesses unique characteristics, such as a low minimum ignition energy and a high burning velocity, which results in combustion behaviors that differ from those of conventional fuels [25–32]. Szwaja et al. investigated hydrogen knocking in a CFR (Cooperative Fuels Research) engine by varying the compression ratio from 4.5 to 17.5 [25]. They identified two knocking modes: light knocking and heavy knocking. Light knocking occurred at compression ratios below 11 and was attributed to hydrogen combustion instabilities initiated by spark discharge in the absence of auto-ignition inside the end-gas. In contrast, heavy knocking occurred at higher compression ratios due to end-gas auto-ignition. They also reported that the intensity of the pressure oscillations is generally associated with the mass of hydrogen consumed by end-gas auto-ignition. Manzoor et al. numerically investigated four combustion modes in a hydrogen spark-ignited engine: normal combustion, knocking, super knocking, and fast flame propagation, corresponding to those observed in CFR engine experiments [26]. They found that the fast flame propagation mode generated pressure oscillations in the absence of end-gas auto-ignition, and a transition from fast flame propagation to detonation was also observed. They further reported that the different combustion modes could be effectively characterized by the relationship between the flame time scale, which is related to the combustion duration, and the ignition delay of the end-gas. Wang et al. studied the end-gas auto-ignition boundaries for hydrogen knocking in a constant-volume vessel [27]. They observed a transition from the non-auto-ignition zone to the critical transition zone and finally to the auto-ignition zone as the pressure and the equivalence ratio increased. They reported that, within the critical zone, the time scales of end-gas auto-ignition chemistry and spark-ignited flame propagation were approximately the same, resulting in a competitive equilibrium for the occurrence of auto-ignition. They concluded that even slight turbulence or mixture inhomogeneities could disrupt this equilibrium, thereby triggering auto-ignition. Li et al. numerically investigated the knocking formation mechanism in a hydrogen direct-injection engine [28]. They demonstrated that pressure-wave-induced compression of the unburned gas promotes low-temperature reactions, accelerating flame propagation and eventually leading to knocking. Other notable studies to interpret knocking phenomena include those of Bradley and colleagues, based on Zeldovich theory [33–35]. They introduced two dimensionless parameters, ξ and ε, during one-dimensional simulations, and presented a ξ-ε diagram that showed whether the propagation mode was deflagration, a developing detonation, or a thermal explosion. Robert et al. [36] performed large-eddy simulations using fuels representative of those of modern gasoline engines. The developing detonation peninsula originally proposed by Bradley et al. [34,35] was reproduced and the two dimensionless parameters characterized the propagation modes appropriately.

Auto-ignition within end-gas can cause knocking and should be avoided during normal operation. However, Konig found that such ignition did not necessarily induce knocking, and suggested that levels of unburned hydrocarbons could be reduced during such combustion [15]. Azimov et al., using a dual-fuel natural gas engine, defined end-gas auto-ignition that was not accompanied by pressure oscillations as PRE-mixed mixture ignition in the end-gas region (PREMIER) combustion [37]. The engine performance and emission characteristics of such combustion were examined. Compared to the levels associated with conventional combustion, both the mean effective pressure and thermal efficiency increased by up to 25%, while carbon monoxide and total hydrocarbon emissions decreased but those of NOx rose. They concluded that PREMIER combustion ensured efficient engine operation. Imamoto et al. investigated the effects of the CO_2 proportion on end-gas auto-ignition when considering cyclic variations during operation of a dual-fuel biogas engine [38]. Mesa et al. examined the PREMIER combustion characteristics of a dual-fuel hydrogen engine under conditions of nitrogen dilution [39]. The operating range of such combustion expanded as the dilution ratio increased because it enhanced the specific heat capacity of the mixture, thereby slowing reaction rates and suppressing formation of the radicals that are essential for auto-ignition. Kawahara et al. used high-speed imaging of a CEM fueled with natural gas to investigate differences in end-gas auto-ignition behavior between PREMIER combustion and knocking [40]. The end-gas auto-ignited area increased faster during knocking than in PREMIER combustion. During knocking, rapid consumption of unburned gas induced a sudden pressure difference between the flame-propagation and end-gas regions that was not apparent during PREMIER combustion because the auto-ignition flame spread relatively slowly. Nirendra et al. investigated how the timing of micro-pilot fuel injection affected end-gas auto-ignition behavior in a dual-fuel natural gas engine. The PREMIER combustion and knocking regimes were clearly distinguishable in the methane-air detonation peninsula [41].

As detailed in the summary above, many studies have explored both knocking and PREMIER combustion. PREMIER combustion is clearly distinct from light knocking proposed by Szwaja et al. [25] in terms of the end-gas auto-ignition occurrence. However, the factors responsible for the difference between the two combustion regimes, specifically the supposedly distinct mechanisms of pressure wave generation and development, remain unclear. Bradley's ξ-ε diagram has been used for numerical simulations of knocking in hydrogen engines [26,31,34]. However, visualization of hydrogen flames is often difficult, and therefore very few studies have collected data on the end-gas auto-ignition of hydrogen–air mixtures under engine-relevant conditions [42]. Even fewer studies have experimentally tested the utility of the ξ-ε diagram.

This study visualized the end-gas auto-ignition of hydrogen–air mixtures and investigated the mechanisms governing the transition from PREMIER combustion to knocking in a dual-fuel hydrogen engine. In an optical CEM, nitrogen-diluted hydrogen–air mixtures were used to generate both PREMIER combustion and knocking at identical mixture compositions. Various KI values were obtained by changing the timing of diesel fuel injection. End-gas auto-ignition was directly visualized using a highly sensitive color camera operating at 57,600 fps while in-cylinder pressure measurements were simultaneously collected. The results indicate a weak correlation between the unburned gas temperature at the onset of end-gas auto-ignition and KI, which, however, tended to increase when an unburned mass fraction was present within the PREMIER combustion regime. In the knocking regime, this mass fraction did not significantly affect pressure wave amplification. Visualization revealed that the spread velocity of the end-gas auto-ignition front was the dominant factor governing KI, which increased with the spread velocity. The experimental results were complemented by calculations using chemical kinetics, and Bradley's theory was then applied to investigate differences in auto-ignition behavior between PREMIER combustion and knocking. On the ξ-ε diagram, a clear transition from PREMIER combustion to knocking was observed. Cycles in which the KI value exceeded 0.3 MPa lay within the developing detonation peninsula.

2. Experimental setup

Fig. 1 shows a schematic diagram of the CEM. The bore and stroke were 92 and 96 mm respectively, and the compression ratio was 17.3:1. The engine was driven by an electric motor and operated at 600 rpm. The in-cylinder pressure signal was measured by a pressure transducer (6052C, Kistler) and amplified by a charge amplifier (Type 5011, Kistler). Table 1 lists the experimental conditions. Given the high compression ratio of the CEM and the elevated reactivity of hydrogen, knocking was readily induced when using a pure hydrogen–air mixture.

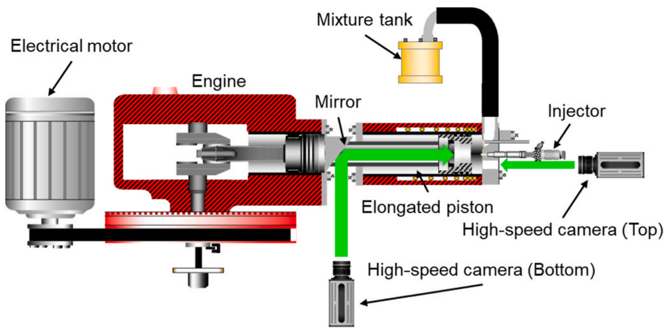

Fig. 1. Schematic diagram of the experimental apparatus.

Table 1
Experimental conditions.

Main fuel	Hydrogen
Equivalence ratio of hydrogen [−]	0.65
Pilot fuel	Diesel oil
Dilution gas	Nitrogen
Dilution ratio [%]	25
Injection timing [deg. ATDC]	−10 ~ −2
Injection pressure [MPa]	50
Injection mass [mg]	0.6
Number of nozzle holes [−]	3
Intake temperature [K]	313
Intake pressure [kPa]	115
Wall temperature [K]	403

Consequently, a control system was required to ensure PREMIER combustion. Mesa et al. investigated the effects of nitrogen dilution on the operating range of a dual-fuel hydrogen gas engine [39], and found that dilution ameliorated the pressure rise by both increasing the specific heat capacity of the charge and moderating the mixture reactivity associated with PREMIER combustion events over a wider range of micro-pilot fuel-injection timings than formerly. In the present study, the mixture composition was adjusted using nitrogen dilution. Tests revealed that a mixture composition of $0.170H_2 + 0.131\ O_2 + 0.699\ N_2$ at an equivalence ratio of 0.65 induced both PREMIER combustion and knocking, and this combination was therefore selected. The dilution ratio was 25%, defined as the molar fraction of the dilution gas in the gas–air mixture. Nitrogen dilution increases the specific heat capacity of the mixture, thereby lowering the peak combustion temperature. The reduced temperature decreases the chemical reactivity of the unburned gas, resulting in a lower flame propagation velocity and a longer ignition delay. Consequently, under the selected mixture conditions, the end-gas reactivity is moderated, allowing variations in the pilot-fuel injection timing to modify the pressure and temperature histories of the end gas and induce a transition from PREMIER combustion to knocking without changing the mixture composition. The mixture was ignited via compression ignition of micro-pilot diesel (0.6 mg). As hydrogen was the primary fuel, any role of diesel was restricted to ignition assistance; therefore, the quantity of diesel was minimized. Diesel was delivered directly to the chamber at a pressure of 50 MPa using a solenoid-controlled injector connected to a common rail system. The injector nozzle with three equally spaced holes was specifically designed to ensure a wide end-gas region. The cylinder wall and mixture were heated to 403 K and 313 K, respectively.

The CEM was equipped with two visualization windows, one located on the piston and one on the cylinder head; these ensured optical access to the combustion chamber. A schematic of the in-cylinder configuration and visualization regions is shown in Fig. 2. The diameters of the visible areas were 22 mm in the top view and 62 mm in the bottom view. A mirror at the base of the elongated piston enabled observations from the bottom. As hydrogen flames exhibit extremely weak luminescence in the

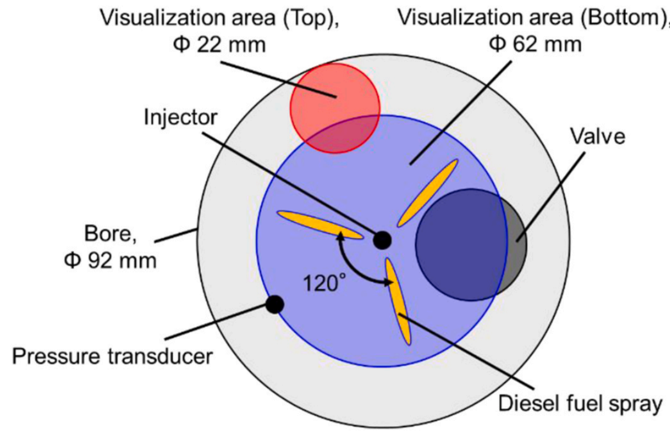

Fig. 2. In-cylinder schematic diagram and visualization area.

visible wavelength range, direct imaging of flame emissions is generally difficult using a conventional camera. In this study, a highly sensitive high-speed color camera (ACS-3, nac Image Technology) was used to image hydrogen flames directly. The camera was equipped with fixed focal length lenses with a remarkably low F-number of 0.85 (VS-50085/C, VS Technology). A second high-speed camera (HX-7s, nac Image Technology) was employed to enable simultaneous visualization of both the top and the bottom, but it was found that this camera lacked the sensitivity required to capture the propagating flame of a hydrogen–air mixture and it was therefore used only to observe the ignition of diesel fuel from the bottom. Representative simultaneous imaging data are shown in Fig. 3. Each optical boundary is indicated by white circles. The bottom-view visualizations illustrate the characteristics of the near-invisible hydrogen flames. Diesel fuel ignition was confirmed, but mixture propagation could not be detected. The luminous flame in the center of the image is thought to reflect soot formation from the diesel fuel. In contrast, in the end-gas region, luminescent hydrogen flames were visualized using the ACS-3. Hydrogen flames emit visible light that originates from excited H_2O, and also faintly exhibit a so-called blue continuum [43,44]; these emissions were captured by the ACS-3 camera. The corner of the piston was chamfered at the boundary between the bottom window and the piston edge; the bright arc is a reflection of the flame-derived luminescence. For the cycles in which the end-gas behavior was visualized using the ACS-3 camera, the frame rate and exposure time were set to 57,600 fps and OPEN, respectively, corresponding to a frame interval of 0.0625 ° CA. The acquired images were stored in 24-bit TIFF format with a resolution of 192× 336 pixels.

Since both PREMIER combustion and knocking are the result of auto-ignition in the end-gas region, it was necessary to determine whether

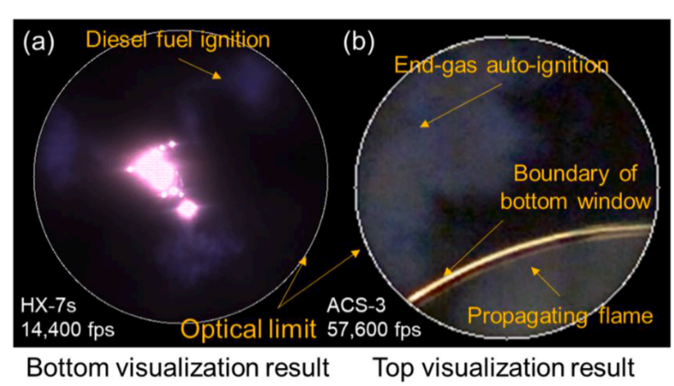

Fig. 3. Simultaneous bottom- and top-view visualization images at the onset of end-gas auto-ignition during knocking: (a) bottom-view image and (b) top-view image.

pressure waves were generated inside the cylinder after auto-ignition; in other words, whether a cycle corresponded to knocking or PREMIER combustion. To classify the combustion regimes, the knocking intensity (KI) was calculated. Because high-frequency pressure oscillations are characteristic of knocking, KI was calculated from the in-cylinder pressure history after application of a 4–20-kHz band-pass filter to remove white noise caused by mechanical vibrations. A Fast Fourier Transform (FFT) method was applied to the in-cylinder pressure data acquired at a sampling frequency of 1 MHz. The desired frequency range was extracted in the frequency domain, and the filtered pressure signal was reconstructed using an inverse FFT (IFFT). The difference between the maximum and minimum values of each filtered pressure history was defined as the KI. PREMIER combustion is defined as a cycle in which end-gas auto-ignition occurs, while no or only negligible pressure oscillations characteristic of knocking are observed, posing no risk of engine damage. Therefore, to reflect this definition, the maximum KI obtained under pilot-fuel-only operation was adopted as the threshold. In the present experimental apparatus, the maximum value of KI obtained during diesel-only operation was 0.05 MPa. Cycles with KI values below this threshold exhibited pressure oscillations comparable to those of normal combustion cycles and therefore did not cause engine damage. In a previous study [38], the same criterion was adopted to define PREMIER combustion in a dual-fuel biogas engine, and the combustion regimes were successfully classified based on the combustion characteristics. Accordingly, 0.05 MPa was adopted as the threshold to distinguish PREMIER combustion from knocking in the present study.

Ignition of diesel fuel initiates mixture combustion; a flame propagates through the combustion chamber, compressing the unburned mixture and resulting in pressure and temperature increases in the end-gas. As the reaction rate generally increases with temperature, the elevated temperature promotes auto-ignition of the unburned mixture. Hence, the temperature of the unburned gas is a key parameter when analyzing end-gas behavior. In this study, this was estimated based on the measured in-cylinder pressure. The non-reacting portion of the compression stroke was approximated as a polytropic process because the pressure–volume relationship during compression is generally well represented by a polytropic relation [45]. Accordingly, the compression stroke between intake valve closing and the onset of pilot-fuel ignition was assumed to follow a polytropic process, as described below:

$$T_1 = T_0\left(\frac{P_1}{P_0}\right)^{\frac{n-1}{n}} \tag{1}$$

The initial gas temperature, T_0, was set to 313 K. The pressure at the time of valve closing was termed P_0. The polytropic index, n, was obtained from the slope of the experimental logP-logV diagram during the compression stroke (−180 to 0 deg. ATDC) under motoring conditions. Based on eight motoring cycles, the average value of n was 1.34 with a standard deviation of 0.04. Thereafter, an adiabatic change was assumed, as shown in Eq. (2):

$$T_2 = T_1\left(\frac{P_2}{P_1}\right)^{\frac{\kappa-1}{\kappa}} \tag{2}$$

where T_1 and P_1 are the estimated temperature and the in-cylinder pressure at the start of combustion, respectively. κ, the specific heat ratio of the mixture, was assumed to be 1.4, given the mixture composition. The estimated unburned-gas temperature was calculated from the bulk in-cylinder pressure. Therefore, it should be interpreted as the mean unburned-gas temperature within the cylinder rather than the local temperature at which end-gas auto-ignition occurs.

Previous studies using gas engines revealed a strong correlation between pressure and rate of heat release (ROHR) histories, and confirmed that ROHR analysis usefully evaluated combustion behavior [38,46]. Hence, ROHR was calculated using the in-cylinder pressure and volume to assess combustion in the CEM:

$$ROHR = \frac{\kappa}{\kappa-1}P\frac{dV}{d\theta} + \frac{1}{\kappa-1}V\frac{dP}{d\theta} \tag{3}$$

P and V are the measured pressure and volume, respectively. Assuming that the mixture is homogeneous, Eq. (3) is derived from the first law of thermodynamics. The effect of the unburned fuel mass on KI was also investigated, as its influence on KI is often debated [15,19,23,25,42]. The mass fraction of unburned fuel at the onset of end-gas auto-ignition was calculated from the ROHR history, as expressed below;

$$\textit{Mass fraction of fuel in the end} - \textit{gas region} = \frac{\sum_{\textit{auto-ignition onset}}^{\textit{combustion end}} ROHR}{\sum_{\textit{combustion start}}^{\textit{combustion end}} ROHR} \times 100 \tag{4}$$

The end-gas auto-ignition timing was defined as the time at which auto-ignition inside the end-gas was first observed in the visualization. The mass fraction of fuel in the end-gas is the amount of combustible mixture remaining in the cylinder at the time of onset of end-gas auto-ignition.

3. Results and discussion

3.1. Pressure and ROHR histories combined with in-cylinder imaging

The experiments visualized end-gas auto-ignition in a hydrogen–air mixture. However, to understand combustion in a dual-fuel hydrogen engine better and to investigate the relationships among the in-cylinder pressure, ROHR, and the visualization data, bottom-view visualization using an ACS-3 camera was first conducted. Fig. 4 shows the pressure and ROHR histories and the visualization results. The frame rate and the exposure time were set to 20,000 fps and OPEN, respectively. In this cycle, diesel fuel was injected at −5 deg. after top dead center (ATDC), resulting in a KI value of 0.034 MPa. This condition was selected to allow observation of the entire process from diesel fuel ignition to end-gas auto-ignition; we initially confirmed that auto-ignition occurred inside the end-gas. Diesel fuel ignition was confirmed at 2.88 deg. ATDC when the ROHR began to increase (image [a]). The fuel was injected in three directions and ignited at approximately 24 mm from the nozzle. Only small differences were observed in the three diesel fuel ignition timings because both the temperature and the mixture distributions in the cylinder were relatively homogeneous. In image (b), both a red luminescence caused by the ignition of the diesel and the propagating flame of the hydrogen–air mixture around the fuel ignition locations can be observed. Combustion of the diesel fuel dominated until approximately 4 deg. ATDC, corresponding to the first ROHR peak, after which the propagating flame became dominant. The diesel ignition initiated the combustion of the hydrogen–air mixture and the flame then started to propagate with increasing pressure and ROHR. Fig. 4 demonstrates that the hydrogen–air premixed flame propagation that could not be detected by the HX-7s camera, as shown in Fig. 3, was successfully visualized by the ACS-3 camera as a result of its approximately 2.5-fold higher color ISO sensitivity and the use of lenses with very low f-numbers (0.85). The luminous flame emission attributable to soot formation is apparent in the upper-right and lower diesel-injection regions of image (c). The ACS-3 camera automatically adjusted the brightness in image (d); the luminosity of the detected flame increased as it propagated. Therefore, the premixed hydrogen–air flame presented as a white luminous emission. Subsequently, a weak but sharp increase in the ROHR was evident at approximately 8.5 deg. ATDC. The visualization image (e) obtained at 9 deg. ATDC suggests that end-gas auto-ignition occurred in the lower-right end-gas region, as luminosity that originated from the end-gas, which was not the same as the light from the propagating flame, was observed. As the KI value of this cycle was 0.034 MPa, and therefore below the knocking threshold of 0.05 MPa, this cycle was classified as PREMIER combustion. The bottom-view visualization series indicates an

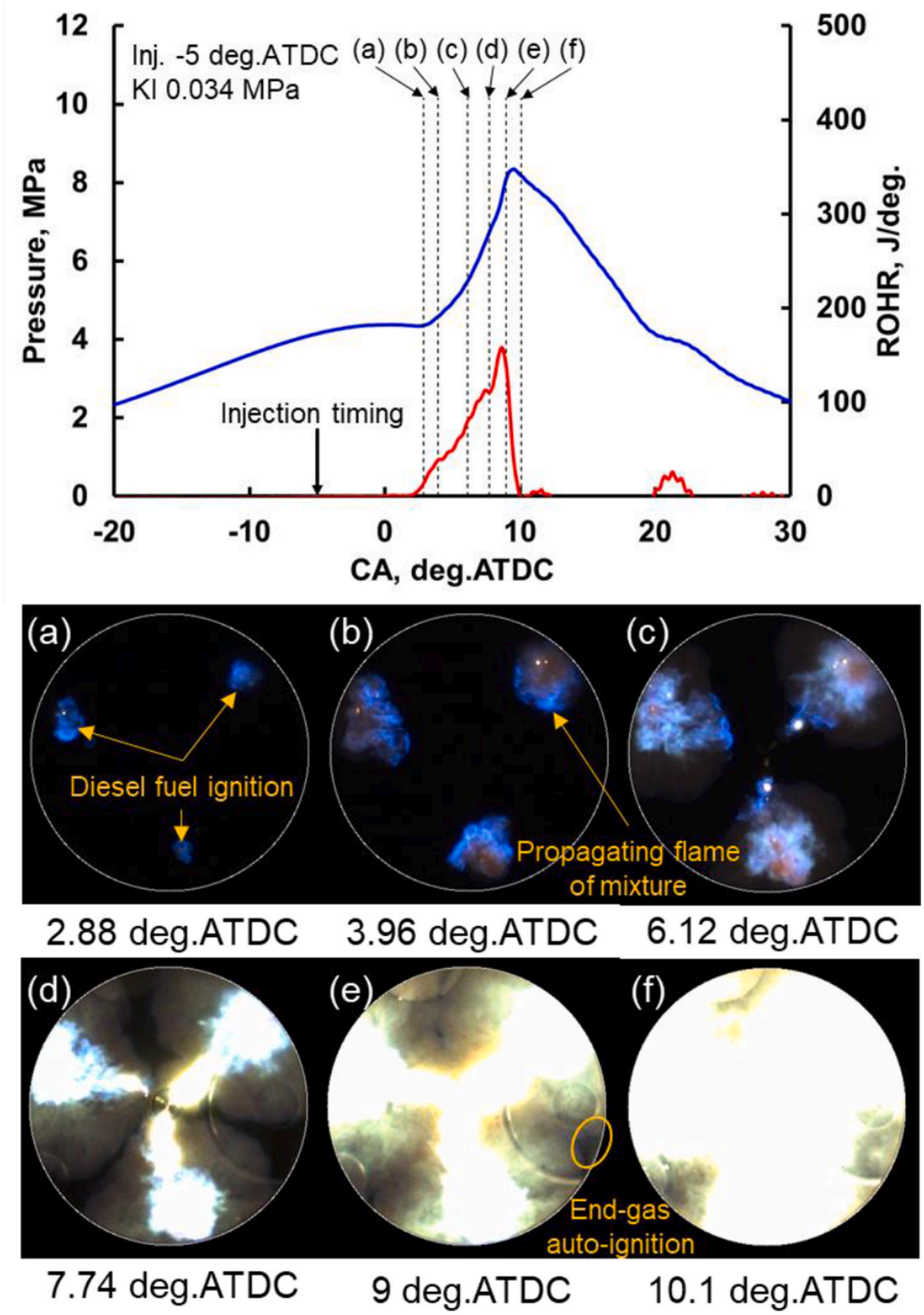

Fig. 4. In-cylinder pressure and ROHR histories and bottom-view visualization images at an injection timing of −5 deg. ATDC.

increase in light emission intensity over time. In image (f), when combustion was near-complete, the entire visible region exhibits a uniform white luminosity, likely because of enhanced thermal radiation from combustion gases attributable to elevations in the in-cylinder temperature and pressure during late combustion. As end-gas auto-ignition was also observed, as shown in image (e), additional top-view visualizations focusing on the end-gas region near the cylinder wall were conducted to investigate end-gas behavior in greater detail.

3.2. Comparison of end-gas auto-ignition during knocking and during PREMIER combustion

Representative profiles of in-cylinder pressure and the ROHRs for normal and PREMIER combustion, and during moderate, strong and severe knocking cycles, are shown in Fig. 5. The diesel fuel injection timings were −2,–6, −8 and −10 deg. ATDC; it was sought to obtain data at varying KI values. Five cycles were obtained under each operating condition, and the cycle-to-cycle variations in each parameter are found in Supplementary materials. Fig. 5 illustrates the significant impact of pilot fuel injection timing on combustion behavior in the dual-fuel hydrogen engine. The ignition delay tended to increase as the diesel fuel injection timing advanced because the ambient pressure and temperature at the time of fuel injection were then lower, allowing more time for fuel–air mixing. Consequently, the premixture level increased prior to diesel fuel ignition, explaining the greater increase in the ROHR immediately after ignition. Advanced diesel fuel injection timing tends to create an earlier combustion phase, a higher peak pressure, and later changes in combustion behavior. Under normal combustion conditions, the gradual increase in the ROHR and subsequent decline indicate that the charge is fully consumed by diesel fuel ignition and diesel-ignited

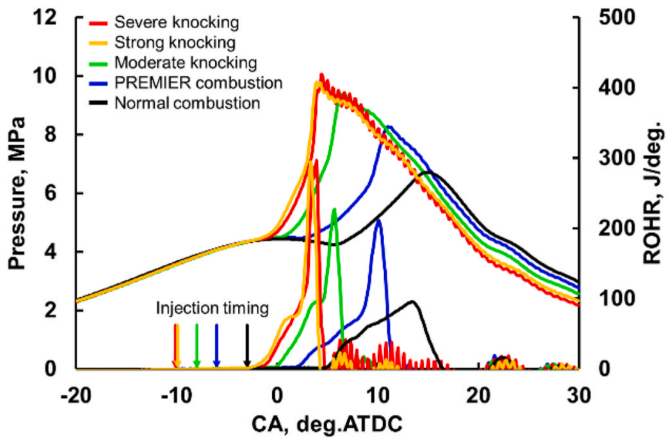

Fig. 5. In-cylinder pressure and ROHR histories under normal combustion, PREMIER combustion, and moderate, strong, and severe knocking conditions.

flame propagation; auto-ignition within the end-gas is absent. In contrast, both PREMIER combustion and the knocking cycles exhibit distinct second increases in the ROHR profile, attributable to end-gas auto-ignition during flame propagation, at approximately 9, 5 and 3 deg. ATDC in each cycle, as revealed by the ROHR profiles. Advanced diesel fuel injection timing was associated with both earlier heat release and advanced pressure rise, increasing both the pressure and temperature of the unburned mixture, thereby promoting auto-ignition within the end-gas. In addition, Fig. 5 shows that earlier end-gas auto-ignition was associated with a larger ROHR peak, indicating increasingly rapid consumption of more unburned gas.

To explore the relationships among the propagating flame, the remaining unburned mixture, and end-gas auto-ignition, top-view visualization focused on the region near the cylinder wall. Fig. 6 shows the results and the pressure histories, filtered via a 4–20-kHz band-pass filter, for the cycles of Fig. 5. Image times are indicated by the circles on the filtered pressure histories. Each image exhibits a bright arc at the boundary between the metal piston edge and the bottom-view window, attributable to reflection of the luminous flame (please see Section 2 above). Image (a) can be initially divided into two regions: a blue-purple region in the lower right, but dark elsewhere. The lower-right image direction is towards the cylinder center. The sequence illustrates the expansion of the blue-purple region containing burned gas, representing mixture flame propagation. The previous dark region holds unburned gas. During a normal combustion cycle, unburned gas was consumed only by the propagating flame initiated via diesel fuel ignition. The KI was then 0.0063 MPa. No pressure oscillations were apparent because the gradual pressure rise associated with flame propagation did not generate any significant pressure imbalance in the cylinder. During a PREMIER combustion cycle, the flame ignited via diesel fuel ignition propagated towards the upper-left direction of image (f). Subsequently (image [g]), luminescence similar to that of the propagating flame is observed in the upper left region, suggesting end-gas auto-ignition onset, because the region was surrounded by only unburned mixture. The time of the end-gas auto-ignition corresponds to that of the second rise in the ROHR history (Fig. 5). During PREMIER combustion, small pressure oscillations developed after end-gas auto-ignition, and the KI value was then 0.048 MPa, below the knocking threshold. Thus, this cycle was classified as PREMIER combustion. Flame propagation and auto-ignition within the end-gas were also observed during knocking cycles. However, during a moderate knocking cycle, the behavior of the propagating flame initiated by diesel fuel ignition differed from that of the other cycles (image [k]); the flame was predominantly located on the right. This was likely attributable to slight variations in the times of ignition of the diesel fuel because it was injected in three directions. A similar trend is observed in image (u). After the auto-ignition observed inside the end-gas in image (k), the subsequent end-gas auto-ignition occurred within the remaining unburned gas region located between the initial end-gas auto-ignition area and the propagating flame in images (l) and (m). In the upper region of image (n), a bright luminosity, likely attributable to engine oil combustion, is apparent on the upper left. The cylinder wall was very close to this region. After the end-gas auto-ignition observed in the images, pressure oscillations occurred during the knocking cycle. Visualization of the end-gas region showed that the pressure oscillations within the chamber were induced by auto-ignition in the end-gas. In image (p), end-gas auto-ignition is observed at almost the same location as in image (k). Subsequently, the auto-ignition spread toward the right, as in a moderate knocking cycle. However, the gas that lay ahead of the end-gas auto-ignition region remained unburned in image (p) but burned in image (k). The visualization data show that more unburned gas was consumed via end-gas auto-ignition as combustion progressed from image (p) to image (t), corresponding to knocking cycles that ranged from moderate to strong. The strong/severe knocking cycles had KI values of 0.23 and 0.55 MPa, respectively. Image (u) shows that the diesel-ignited flame propagated from the bottom left region. Subsequently, auto-ignition inside the end-gas occurred at the center, and a large unburned region remained ahead. Thereafter, the unburned gas was rapidly consumed via successive end-gas auto-ignitions, followed by severe pressure oscillations.

As it has been suggested that the spatial relationship between end-gas auto-ignition and unburned gas is closely related with KI, this relationship was further investigated. Fig. 7 shows the end-gas auto-ignition locations and selected visualization data at auto-ignition onset. In Fig. 7 (a), the plots indicate the locations where auto-ignition inside the end-gas was first observed in each cycle, and the plot colors show the corresponding KI values. Blue points represent KI values below 0.05 MPa, indicating PREMIER combustion. Knocking cycles are marked by the green points with KI values of 0.05–0.2 MPa and red points with KI values exceeding 0.2 MPa. Fig. 7 (a) shows that auto-ignition inside the end-gas occurred both near the upper boundary of the visualization window and closer to the center, thus adjacent to the cylinder wall and ahead of the flame front. However, the KI tended to be higher when the end-gas auto-ignition occurred closer to the center of the image. This may be attributable to pressure wave reflection at the cylinder wall. Previous studies have suggested that pressure waves are reflected by the chamber wall and subsequently amplified [22,47]. The pressure wave development in the present study may be similar. After such waves have been generated ahead of the propagating flame and then propagated towards the wall through the unburned region, they may have been amplified by reflection from the wall. However, in some cycles, although end-gas auto-ignition occurred at similar locations, the subsequent combustion behavior differed, associated with either knocking or PREMIER combustion. Fig. 7 (b) shows the visualization data at the onset of auto-ignition inside the end-gas for the cycles indicated in Fig. 7 (a). These compare the knocking and PREMIER combustion cycles in which the end-gas auto-ignition locations are relatively similar. The fronts of propagating flames initiated via diesel fuel ignition are indicated by red lines. Image (A) shows that the burned gas produced by the diesel-ignited propagating flame occupied most of the visualization region at the time of end-gas auto-ignition. Although the end-gas auto-ignition locations were near-identical, most gas in image (D) remained unburned. Images (B) and (E) indicate that similar proportions of burned gas were consumed by the propagating flame; however, an unburned region is visible on the lower right only in image (E), attributable to differences in flame propagation behavior. Image (F) also shows a residual unburned region on the lower left that is not seen in image (C). Fig. 7 suggests that the relative spatial relationship between the end-gas auto-ignition location and the surrounding unburned region plays an important role in terms of pressure wave generation. The numerical simulations of Terashima et al. revealed that the pressure wave propagates in the unburned gas region and is amplified by the heat released by

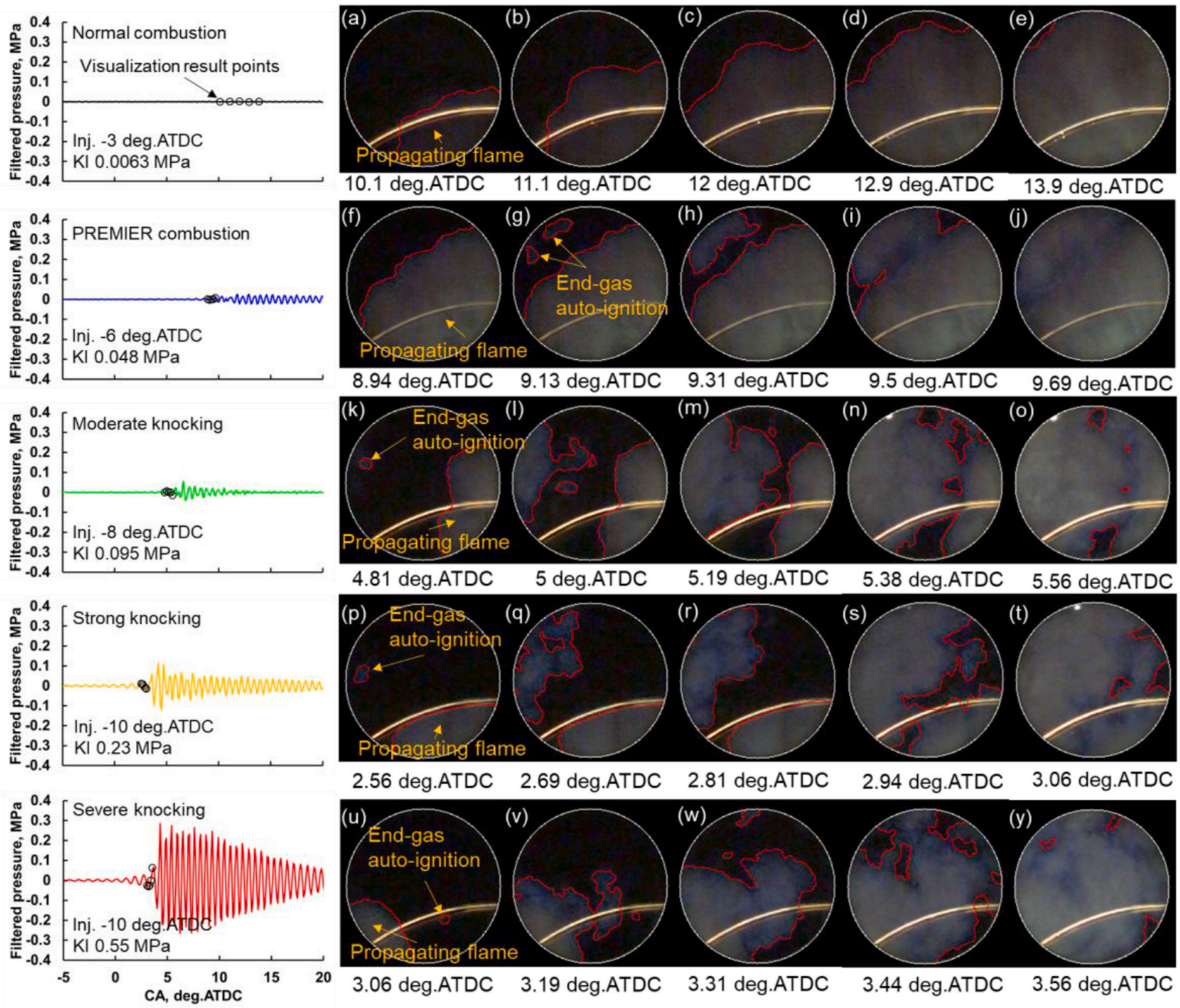

Fig. 6. 4–20 kHz band-pass filtered pressure histories and top-view visualization images under normal combustion (a–e), PREMIER combustion (f–j), and moderate (k–o), strong (p–t), and severe (u–y) knocking conditions. The red contours in the images represent the boundaries between the burned and unburned regions. The bright arc observed in the images represents a reflection of the flame-derived luminescence. (For interpretation of the references to color in this figure legend, the reader is referred to the Web version of this article.)

the chemical reaction behind the wave [22]. Although the visualization range is limited, a similar trend is observed in Figs. 6 and 7. When more unburned gas remained ahead of the auto-ignition area, the pressure waves generated were amplified as they propagated through this region, resulting in a higher KI value. The visualization data suggest that such waves may be amplified via wall reflection and the energy input from end-gas auto-ignition.

Fig. 6 also shows variations in the spread behavior of the end-gas auto-ignition flame. As the KI increased, that flame tended to spread more rapidly. During PREMIER combustion, after auto-ignition inside the end-gas [confirmed in image (g)], both subsequent end-gas auto-ignition in the remaining unburned region ahead of the initial auto-ignition area and propagation of end-gas auto-ignition flames are observed from image (h) to image (j). Propagation appears to play the dominant role in terms of flame spread. The results suggest that a local pressure rise attributable to end-gas auto-ignition was less likely during PREMIER combustion than under other conditions, as the end-gas tended to be primarily consumed via flame propagation. This prevented rapid energy release in the end-gas and the development of any significant pressure imbalance in the chamber, resulting in no or small pressure oscillations during PREMIER combustion. On the other hand, during knocking cycles, the end-gas auto-ignition flame apparently propagated rapidly via sequential end-gas auto-ignition rather than flame propagation *per se*, and this became more pronounced as KI increased. In particular, during the severe knocking cycle shown in Fig. 6, propagation of the end-gas auto-ignition flame was barely observable. Therefore, differences in the mode of flame spread following end-gas auto-ignition—whether unburned gas was consumed by successive auto-ignitions inside the end-gas or by propagation of the auto-ignition flame—were associated with variations in the spread velocity of the end-gas auto-ignition flame and the subsequent pressure oscillations.

As the spread behavior of the end-gas auto-ignition flame influenced the subsequent pressure waves, the spread velocity of the auto-ignition front was estimated using the visualization data. The procedure

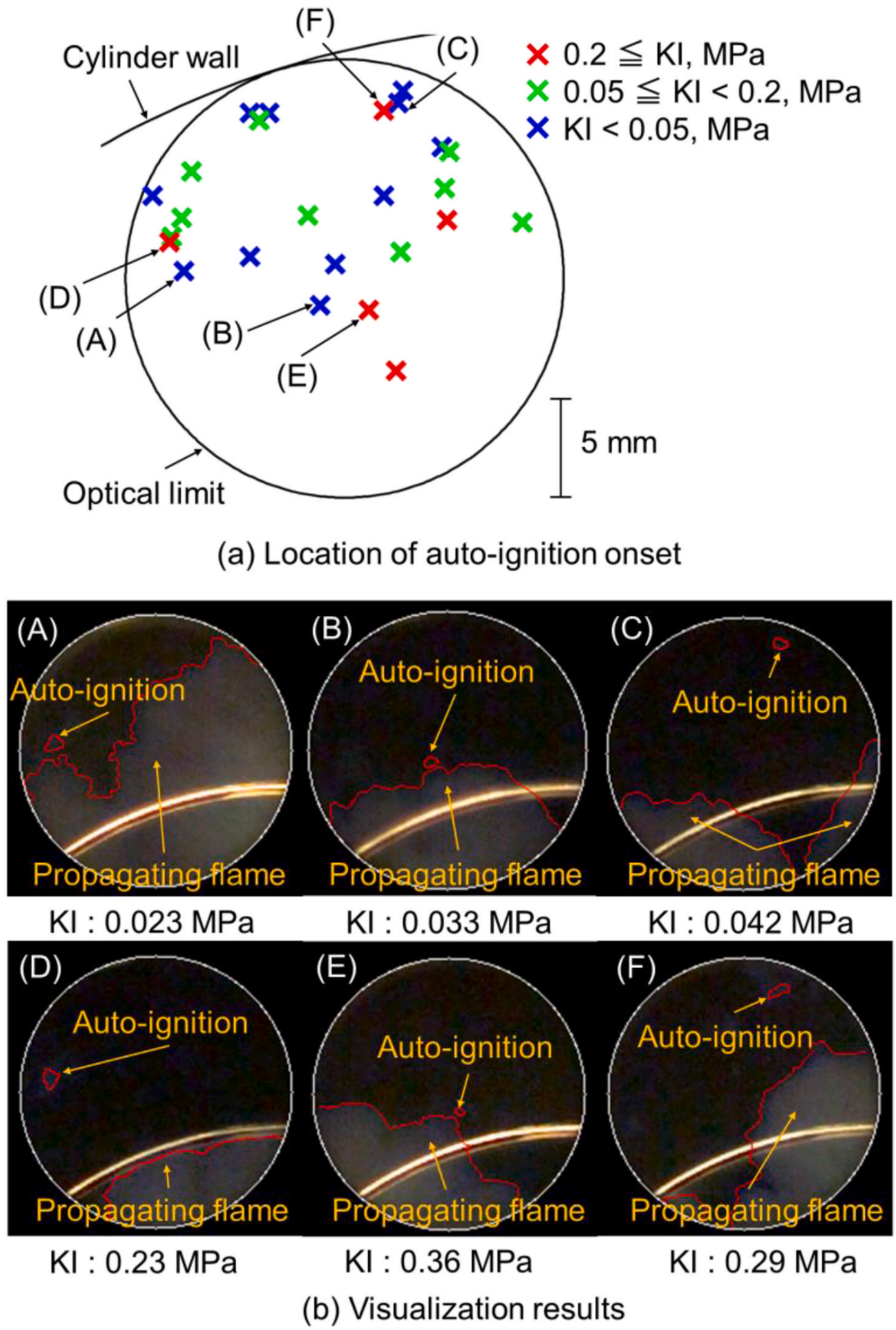

Fig. 7. (a) Spatial distribution of initial end-gas auto-ignition locations and (b) corresponding top-view visualization images at the onset of auto-ignition. The red contours in the images represent the boundaries between the burned and unburned regions. (For interpretation of the references to color in this figure legend, the reader is referred to the Web version of this article.)

employed is shown in Fig. 8. Binarized images were generated from the blue-channel images using the method of Otsu [48], and the end-gas auto-ignition flame regions were identified. The blue channel was selected because it most clearly reproduced the end-gas auto-ignition flame after binarization. Subsequently, the flame edge was located. This procedure was applied to multiple consecutive images when calculating the distance from the end-gas auto-ignition edge initially detected within the visualization region. The distance was then converted to a velocity based on the frame rate and the spatial resolution of the images. When the end-gas auto-ignition flame overlapped with the propagating flame or with the bright arc between the metal piston and the bottom-view window in the image, edge detection became difficult. In such cases, the edge was estimated visually from the image sequence. The spatial resolution was 0.12 mm/pixel, and the width of the bright arc observed in the images was approximately 5 pixels, resulting in a maximum uncertainty in the estimated velocity of approximately ± 17 m/s. This uncertainty has a limited impact on the representative spread velocities of approximately 100 m/s and 400 m/s presented below. The spread velocity was evaluated over ten consecutive images because the auto-ignition flame required up to ten images to spread from its initial appearance to the boundary of the visualization region. The purpose of this image analysis was to investigate the relationship

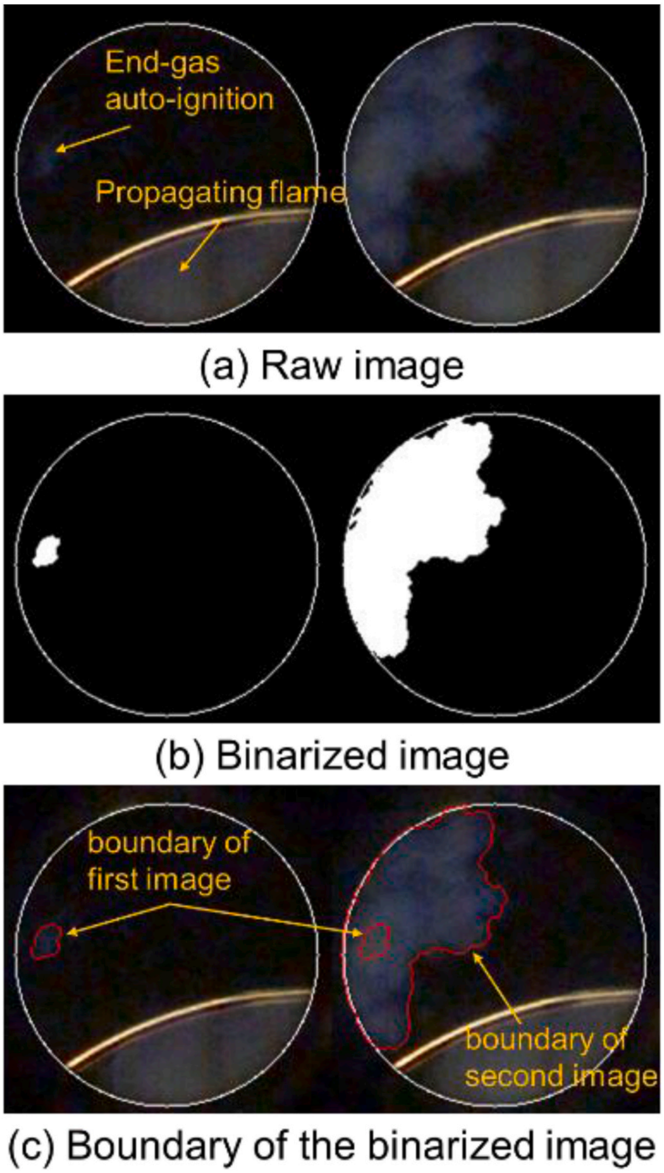

Fig. 8. Image processing flow for a series of visualization results: (a) raw images, (b) binarized images detected as auto-ignition flame and (c) boundary of the binarized images. The red contours represent the boundaries between the burned and unburned regions. (For interpretation of the references to color in this figure legend, the reader is referred to the Web version of this article.)

between the characteristics of end-gas auto-ignition flames and the development of pressure waves. The pressure waves in knocking cycles are attributable to localized pressure rises caused by the rapid energy release of end-gas auto-ignition [22,34,49]. Bradley et al. suggested that pressure wave development was strongly influenced by energy release during auto-ignition [34]. As the end-gas auto-ignition spread subsonically in the present study, the energy supplied to pressure waves would be expected to be dominated by the fastest spread velocity of the end-gas auto-ignition. Accordingly, this velocity was used in calculations, as it represented the most significant local contribution of end-gas auto--ignition to pressure wave development.

Fig. 9 shows the relationships among KI, the unburned gas temperature, the mass fraction of unburned fuel at the onset of end-gas auto-ignition, and the spread velocity of the auto-ignition front. The color of the plot indicates the KI value. Unburned gas temperatures were calculated using Eqs. (1) and (2) and unburned mass fractions were derived employing Eq. (4). The estimated unburned gas temperature at the onset of end-gas auto-ignition was 910–960 K. The auto-ignition temperature of hydrogen is 858 K at 298 K and 1 atm [2]. The temperature of the unburned gas plays a significant role in the onset of end-gas auto-ignition, as an unburned mixture does not auto-ignite at low temperatures. The temperatures were 915–945 and 915–960 K during PREMIER combustion and knocking cycles, respectively. A modest increase in the KI value with increasing temperature was observed; however, the trend was weak, indicating that the end-gas temperature exerted only a limited impact on pressure wave development. The unburned mass fraction data indicate behavior that differed from that of temperature. When the fuel mass fraction in the end-gas was below approximately 50%, most cycles featured PREMIER combustion; the KI tended to increase as the fuel mass fraction rose, and knocking cycles predominated at values above 50%. However, the KI values were widely distributed within this range, and there was no clear correlation between KI and the unburned fuel mass fraction. Although KI values consistently rose slightly with increasing temperature, the mass fraction data showed that the KI increased with larger mass fractions over the PREMIER combustion range. However, in the knocking regime, an increase in mass fraction was not associated with a rise in KI. This implies that the amount of unburned fuel in the end-gas affects pressure wave generation after auto-ignition onset. In other words, the cycle may have been classified as PREMIER combustion or knocking, but this did not significantly affect the pressure wave amplitude. In contrast, the KI increased as the spread velocity of the end-gas auto-ignition flame front rose. Cycles with velocities below approximately 100 m/s were associated with PREMIER combustion. Under severe knocking conditions, with KI attaining 0.55 MPa, the spread velocity was approximately 400 m/s; such rapid spread is unlikely to be explained solely by reference to the parameters of conventional flame propagation. As shown in Fig. 6, the coexistence of successive end-gas auto-ignition events, combined with propagation of the auto-ignition flame, contributed to the rapid spread velocity.

Fig. 9 indicates that the rate of fuel consumption attributable to auto-ignition, not the total burned mass in the end-gas, played the more significant role in terms of subsequent pressure wave development. This implies that strong oscillations in pressure could be mitigated by suppressing rapid propagation of the end-gas auto-ignition front. Figs. 6, 7, and 9 show that the spatial relationships between the locations of the unburned mixture and end-gas auto-ignition, and the subsequent spread of the end-gas auto-ignition front, create pressure waves. The presence of a large amount of unburned fuel is not relevant in this context.

3.3. *Analysis of end-gas auto-ignition characteristics based on Bradley's theory*

To investigate the mechanisms that might explain the differences in end-gas auto-ignition behavior, the theory proposed by Bradley et al. [34,35] was used to evaluate the experimental results. The findings are summarized below.

When the ignition delay τ_i was spatially distributed, ignition occurred at different times and sites, resulting in (apparent) flame propagation. Considering only one-dimensional propagation, the velocity of the auto-ignition front relative to the unburned gas, u_a, which is inversely proportional to the ignition delay gradient, is expressed as follows [33]:

$$u_a = \left(\frac{d\tau_i}{dx}\right)^{-1} \tag{5}$$

Considering both burned gas expansion and mass conservation, the propagation velocity relative to the fixed stationary coordinate, dx/dt, is given by Eq. (6):

$$\frac{dx}{dt} = u_a\sigma \tag{6}$$

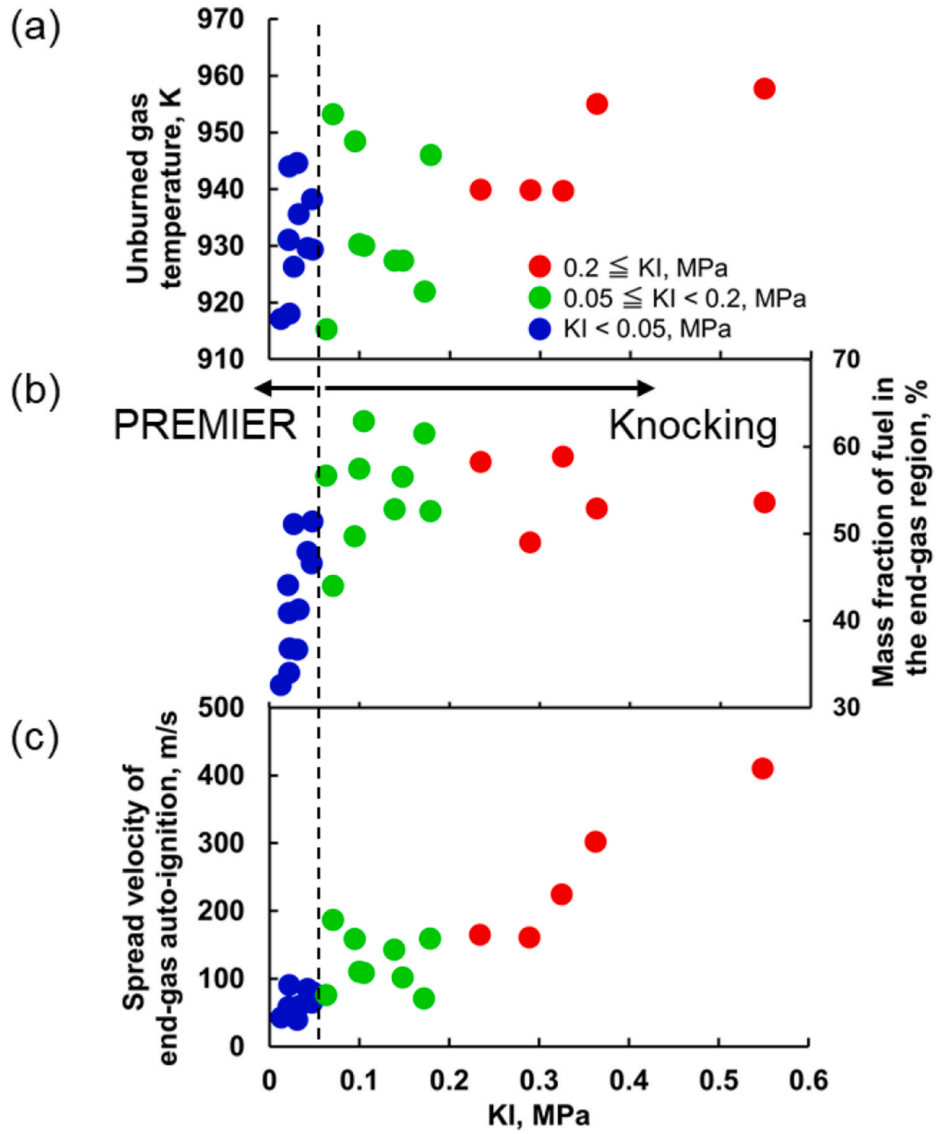

Fig. 9. Relationships among KI, (a) unburned gas temperature, (b) mass fraction of unburned fuel at the onset of end-gas auto-ignition and (c) spread velocity of end-gas auto-ignition.

where σ is the density ratio of unburned to burned gas. Eq. (5) is next transformed into Eq. (7) using the temperature derivative of the ignition delay, τ_i/dT , and the temperature gradient, dT/dx:

$$u_a = \left(\frac{d\tau_i}{dT}\frac{dT}{dx}\right)^{-1} \tag{7}$$

If u_a attains the acoustic velocity, a, under the critical temperature gradient $(dT/dx)_C$, the pressure wave and the auto-ignition front can be reinforced, creating to the development of detonation:

$$\left(\frac{dT}{dx}\right)_C = a^{-1}\left(\frac{d\tau_i}{dT}\right)^{-1} \tag{8}$$

A first dimensionless parameter, ξ, can be introduced by normalizing the actual temperature gradient with the critical temperature gradient, as shown by Eq. (9):

$$\xi = \frac{\frac{dT}{dx}}{\left(\frac{dT}{dx}\right)_C} \tag{9}$$

Using Eqs. (7) and (8), Eq. (9) is transformed into Eq. (10):

$$\xi = \frac{a}{u_a} \tag{10}$$

In addition, Bradley et al. defined ε when considering the effect of chemical energy unloaded into the acoustic wave at the hot spot, as expressed by Eq. (11):

$$\varepsilon = \frac{\frac{r_0}{a}}{\tau_e} \tag{11}$$

where ε is the ratio of the time when the acoustic wave propagates through the hot spot radius, r_0, to the excitation time, τ_e. Bradley et al. reported that the combustion mode at the hot spot (deflagration, developing detonation, or thermal explosion) could be predicted using the two dimensionless parameters. The interactions between the pressure waves, the auto-ignition front, and the mixture reactivity are important when seeking to understand PREMIER combustion, Bradley's theory effectively interpreted the phenomena observed in the present study. Therefore, the two parameters were estimated experimentally.

To calculate ξ and ε, the acoustic velocity, a, was derived using Eq.

(12):

$$a = \sqrt{\kappa RT} \tag{12}$$

where κ and R are the specific heat ratio and the gas constant, respectively, and T is the unburned gas temperature at the onset of auto-ignition. The spread velocity of the end-gas auto-ignition front was employed when calculating dx/dt. The density ratio and excitation time were derived using the KUCRS chemical kinetics for hydrogen of CHEMKIN-Pro software [50,51]. Fig. 10 illustrates how the excitation time was calculated. That time was defined as the interval between the times at which the ROHR attained 5% of its maximum value and the time at which it attained its maximum value [52]. The pressure and temperature data used in the calculations were the experimental values at the onset of end-gas auto-ignition. As it was difficult to estimate the radius of the hot spot experimentally, it was assumed to be half of the top dead center (TDC) clearance (3.5 mm). Given the possible integral-length scale of turbulence at TDC, Kalghatgi assumed a hot spot radius of 5 mm, which is similar to the present value [53].

To investigate the effect of the interaction between pressure waves and the auto-ignition front on KI, the estimated values of ξ are plotted against KI values in Fig. 11. The KI increased exponentially as ξ decreased. According to Eq. (10), when ξ exceeds unity, a decrease in ξ indicates that the velocity of the auto-ignition front approaches that of the acoustic wave, thereby strengthening the front/wave interaction and enhancing pressure wave amplification. Such results suggest that the velocity of the auto-ignition flame plays a key role in the development of pressure waves. A similar trend has also been reported in previous studies [21,54]. To analyze the experimental results further based on Bradley's theory, ξ is plotted against ε in Fig. 12, and Table 2 presents the estimated parameters for the cycles of Fig. 5. The values of ε are concentrated around 7 because the variations in excitation time and acoustic velocity were both small, with ranges of 0.69–0.8 μs and 650–680 m/s, respectively. In contrast, the estimated ξ covers a wide range of values. PREMIER combustion occurred when ξ exceeded 20. PREMIER combustion and knocking coexisted at a ξ value of around 18, whereas only knocking was observed below this value. Cycles with KI values of around 0.2 MPa lay near the boundary of the developing detonation peninsula. When the KI value exceeded 0.3 MPa, some points appeared inside the peninsula. In this study, ξ was estimated from u_a and a as expressed by Eq. (10). However, as the acoustic velocity did not vary significantly, the velocity of the auto-ignition flame is considered to be the dominant factor determining ξ.

The auto-ignition front velocities (u_a values) were determined from the visualization data. As shown in Eq. (7), u_a is derived from the temperature gradient and the temperature sensitivity of the ignition delay.

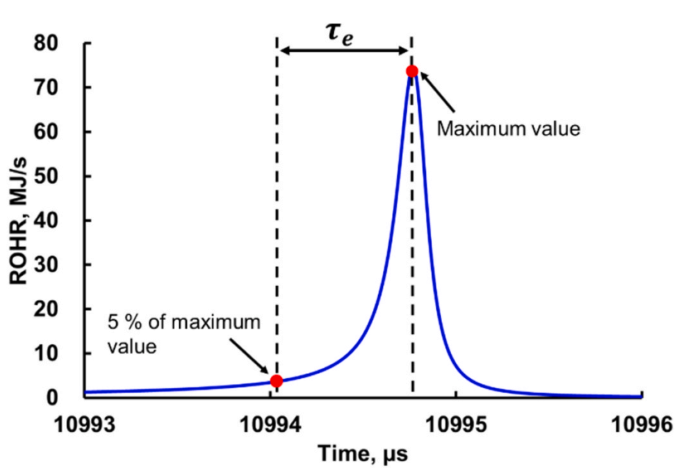

Fig. 10. Definition of the excitation time obtained from chemical kinetics calculations.

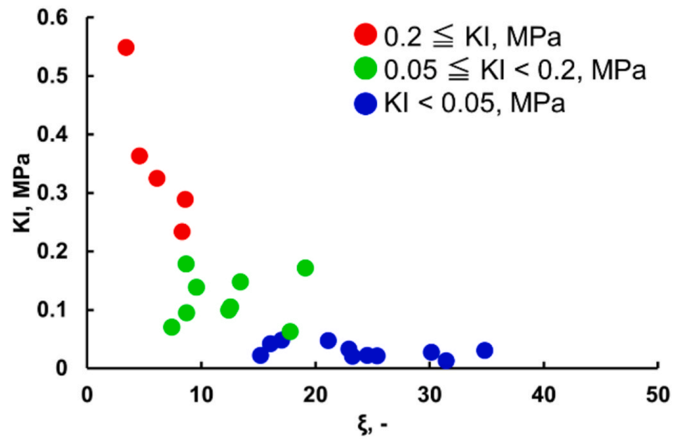

Fig. 11. Relationship between KI and ξ

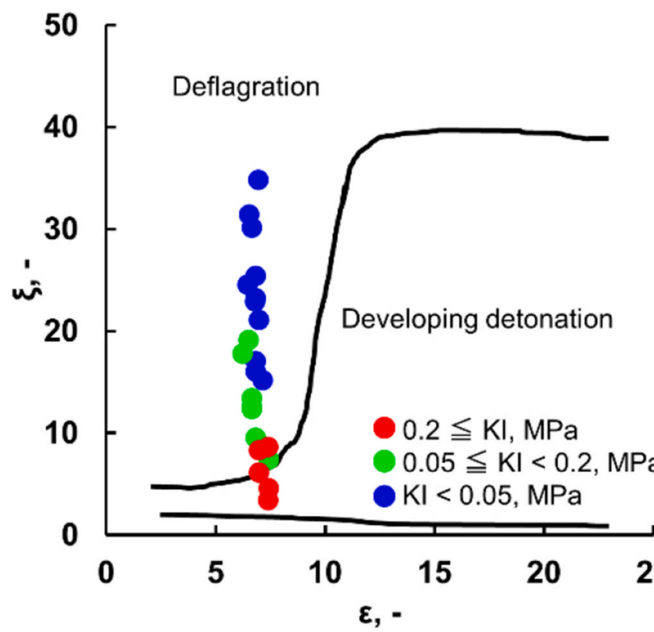

Fig. 12. Experimental results plotted on the $\xi - \varepsilon$ diagram proposed by Bradley [34].

Hence, that delay was estimated using CHEMKIN-Pro software. Fig. 13 shows that delay and the temperature sensitivity thereof. The ignition delay was defined as the time at which the slope of the temperature profile attained its maximum value. This delay decreased monotonically with increasing temperature. The temperature derivative of the ignition delay obtained from the chemical kinetic calculations and the auto-ignition front velocity, u_a, were used in Eq. (7) to estimate the temperature gradient at the hot spot. The relationships among KI, the temperature sensitivity of the ignition delay, and the temperature gradient, are shown in Fig. 14, where the KI increases as the temperature gradient and the derivative of the ignition delay approach 0 ms/K and 0 K/mm, respectively. Notably, this tendency is more affected by the temperature gradient than by the gradient of the ignition delay. As KI increases, the temperature gradient increases asymptotically toward 0 K/mm. Therefore, that gradient at the hot spot appears to play a dominant role in terms of the end-gas auto-ignition behavior observed in this study. However, the temperature gradients estimated here were much smaller than those suggested by Kalghatgi et al. [53], who used a value of −2 K/mm when illustrating the general effects of such gradients on knocking, whereas in our experiments the values were of the order

Table 2
Estimated parameters for r_0 = 3.5 mm under normal combustion, PREMIER combustion, and moderate, strong, and severe knocking conditions.

	KI [MPa]	P [MPa]	T [K]	a [m/s]	dx/dt [m/s]	τ_e [μs]	ξ [−]	ε [−]	τ_i [ms]	$d\tau_i/dT$ [ms/K]	dT/d x [K/mm]
PREMIER combustion	0.048	6.22	929	670	80	0.76	17	6.83	16.4	−0.40	−0.063
Moderate knocking	0.095	6.93	949	677	159	0.71	8.7	7.23	9.6	−0.23	−0.057
Strong knocking	0.23	6.60	940	674	165	0.74	8.3	6.97	12.2	−0.29	−0.042
Severe knocking	0.55	6.86	958	680	410	0.69	3.4	7.40	7.8	−0.18	−0.028

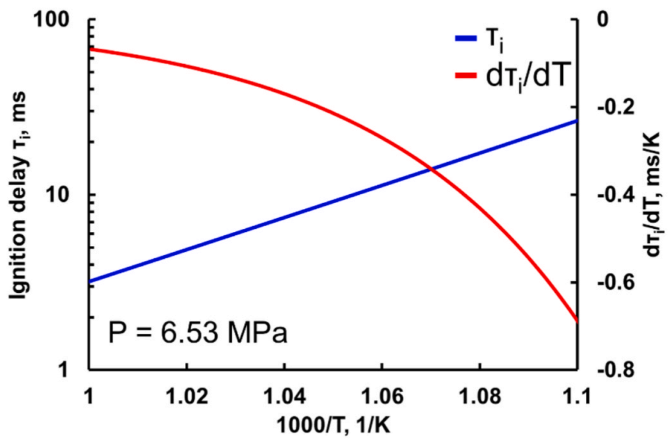

Fig. 13. Ignition delay and temperature sensitivity of ignition delay at a pressure of 6.53 MPa.

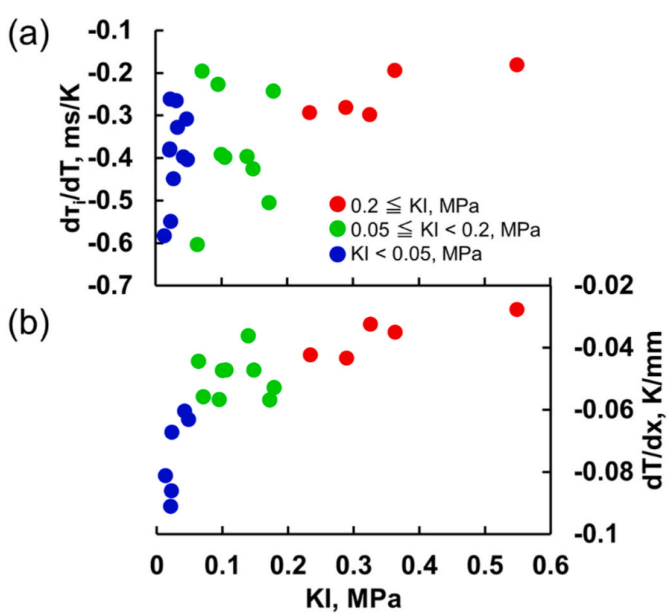

Fig. 14. Relationships among KI, (a) temperature gradient and (b) ignition delay gradient.

−0.01K/mm, suggesting near-homogeneous temperature distributions. The estimated temperature gradients are much smaller than those generally be expected under engine relevant conditions. Therefore, the absolute values of the estimated temperature gradients should be interpreted with caution. This discrepancy may be attributable to either a difference in the ignition delay between the simplified calculated conditions and the actual in-cylinder environment or/and underestimation of the hot spot temperature. The calculations of ignition delay employed a zero-dimensional homogeneous assumption, whereas the environment of a real engine features turbulence and spatial inhomogeneities in both temperature and mixture concentration. Such inhomogeneities may create localized regions with shorter ignition delays, and auto-ignition onset might be affected by the conditions of the most reactive zones rather than the spatial averages. This means that the ignition delay evaluated using a homogeneous assumption may differ from that in the actual end-gas. Liu et al. reported that turbulence created a difference between experimental and calculated ignition delays [18]. Indeed, even the shortest ignition delay calculated in the present study was about 8 ms (corresponding to 28.8 deg. CA), which is considerably longer than the ignition delay expected under engine knocking conditions. As the ignition delay increased, the sensitivity of that delay to temperature became larger (Fig. 13). Consequently, the temperature gradient derived from Eq. (7) tended to fall. In this study, the pressure used for temperature estimation was measured close to the cylinder center, whereas the auto-ignition observed in the visualization window occurred in end-gas closer to the cylinder wall, where unburned gas might have experienced additional compression attributable to flame propagation. Thus, the local thermodynamic conditions in the end-gas might have differed from those at the measurement site. Furthermore, However, such effects would not be expected to influence the overall results systematically. Therefore, the relative differences in the derivatives of the ignition delays and the temperature gradients, and their effects on end-gas auto-ignition behavior, can be meaningfully discussed. Despite the limited quantitative accuracy of the local temperature and ignition delay estimates at the hot spot, the present approach offers useful qualitative insights into the relationship between hot spot conditions, PREMIER combustion, and knocking.

In this study, the experimental results were explored based on the theory proposed by Bradley et al. [34,35]. The ξ-ε diagram in Fig. 12 indicates a transition of the combustion mode from PREMIER combustion to knocking. As KI increased, ξ decreased, approaching the developing detonation peninsula. When KI exceeded 0.3 MPa, the corresponding cycles lay within that peninsula. The estimated value of ξ strongly depended on the velocity of the auto-ignition front relative to the unburned gas, u_a, as revealed by the visualization data. This suggests that the spread velocity of the end-gas auto-ignition flame significantly impacted KI. Note that u_a values can be obtained experimentally even in hydrogen–air mixtures, in which visualization of end-gas auto-ignition flames is generally considered difficult. This study provides the novel insights into end-gas auto-ignition in hydrogen-air mixtures. Further investigations over a wider range of operating conditions are therefore required to verify the generality of the present findings.

4. Conclusions

In this study, end-gas auto-ignition in hydrogen–air mixtures was visualized in an optical CEM under both knocking and PREMIER combustion. Various KI values were obtained by changing the timing of diesel pilot fuel injection. To investigate the transition from PREMIER combustion to knocking, the factors that affect KI were examined using thermodynamic analysis, image processing, and Bradley theory. The main conclusions can be summarized as follows.

1. End-gas auto-ignition in various hydrogen–air mixtures was visualized directly using a high-speed, highly sensitive color camera equipped with lenses of an extremely low f-number (0.85). During PREMIER combustion cycles, the end-gas auto-ignition flame spread via an interaction between flame propagation and sequential auto-

ignition onset. During knocking, the spread of the end-gas auto-ignition flame was driven primarily by auto-ignition onsets, and the auto-ignition flame proceeded more rapidly.

2. A weak correlation was apparent between KI and the temperature of the unburned gas at the onset of end-gas auto-ignition. In the PREMIER combustion regime, the mass fraction of fuel in the end-gas region increased with the KI. In contrast, under knocking conditions, the unburned mass fraction exhibited no clear relationship with KI, suggesting that this fraction influences mainly pressure wave initiation, not amplification. The spread velocity of the end-gas auto-ignition was the dominant parameter governing KI. The spread velocity remained below 100 m/s during PREMIER combustion, but attained approximately 400 m/s in severe knocking cycles.
3. The theory proposed by Bradley et al. [34,35] was used to evaluate the experimental results, and two dimensionless parameters, ξ and ε, were estimated. On the ξ-ε diagram, a clear transition from PREMIER combustion to knocking was observed. As KI exceeded 0.3 MPa, the corresponding cycles lay inside the developing detonation peninsula. The results also indicate that the temperature gradient at the hot spot played a key role in terms of the rapid spread of the end-gas auto--ignition front and subsequent pressure wave development.

CRediT authorship contribution statement

Riku Okamoto: Investigation, Methodology, Validation, Visualization, Writing – original draft. **Nobuyuki Kawahara:** Conceptualization, Funding acquisition, Project administration, Supervision, Writing – review & editing. **Yoshimitsu Kobashi:** Validation, Visualization, Writing – review & editing.

Declaration of competing interests

The authors declare that they have no known competing financial interests or personal relationships that could have appeared to influence the work reported in this paper.

Acknowledgement

This work was supported by JSPS KAKENHI Grant Number 25K08147.

Appendix A. Supplementary data

Supplementary data to this article can be found online at https://doi.org/10.1016/j.ijhydene.2026.157103.

Nomenclature

Abbreviations

ATDC After Top Dead Center
CA Crank Angle
CEM Compression and Expansion Machine
KI Knocking Intensity
PREMIER PREmixed Mixture Ignition in the End-gas Region
ROHR Rate of Heat Release
TDC Top Dead Center

Symbols

u_a Velocity of the auto-ignition front relative to that of unburned gas
a Acoustic velocity
τ_i Ignition delay
dx/dt Velocity of the auto-ignition front relative to the fixed stationary coordinate
σ Density ratio
$(dT/dx)_C$ Critical temperature gradient
ξ Dimensionless temperature gradient at a hot spot
ε Dimensionless hot spot reactivity
r_0 Initial hot spot radius
τ_e Excitation time

References

[1] Shahi MI, et al. Hydrogen production techniques and use of hydrogen in internal combustion engine: a comprehensive review. Fuel 2024;378:132769.
[2] White CM, et al. The hydrogen-fueled internal combustion engines: a technical review. Int J Hydrogen Energy 2006;31:1292–305.
[3] Bao J, et al. Comparative analysis of chamber dimension and recess location on combustion behavior in a rotary engine with hydrogen addition. Fuel 2026;404:136392.
[4] Ma Q, et al. Multi-objective optimization of a hydrogen-butanol rotary engine driven by machine learning and intelligent algorithm. Appl Therm Eng 2026;300:131560.
[5] Hosseini SH, et al. Use of hydrogen in dual-fuel diesel engine. Prog Energy Combust Sci 2023;98:101100.
[6] Deb M, et al. An experimental study on combustion, performance and emission analysis of a single cylinder, 4-stroke DI-diesel engine using hydrogen in dual fuel mode of operation. Int J Hydrogen Energy 2015;40:8586–98.
[7] Tsujimura T, et al. The utilization of hydrogen in hydrogen/diesel dual fuel engine. Int J Hydrogen Energy 2017;42:14019–29.
[8] Dimitriou P, et al. Low-load hydrogen-diesel dual-fuel engine operation – a combustion efficiency improvement approach. Int J Hydrogen Energy 2019;44:17048–60.
[9] Bawne SK, et al. Thermodynamic investigation of hydrogen-enriched diesel dual-fuel CI engine through first and second law analysis. Int J Hydrogen Energy 2026;227:154561.
[10] Shafee SM, et al. A comprehensive review of hydrogen integration in advanced engine modes. Next Energy 2025;9:100394.
[11] Wang Z, et al. Knocking combustion in spark-ignition engines. Prog Energy Combust Sci 2017;61:78–112.
[12] Pöschl M, et al. Influence of temperature inhomogeneities on knocking combustion. Combust Flame 2008;153:562–73.
[13] Kawahara N, et al. Auto-ignited kernels during knocking combustion in a spark-ignition engine. Proc Combust Inst 2007;31:2999–3006.
[14] Qi Y, et al. Effects of thermodynamic conditions on the end gas combustion mode associated with engine knock. Combust Flame 2015;162:4119–28.

[15] Konig G, et al. End gas autoignition and knock in a spark ignition engine. SAE 1990:902135.
[16] R. Schießl et al., "Double-pulse PLIF imaging of self-ignition centers in an SI engine", SAE 2001-01-1925.
[17] Wang Z, et al. Analysis of pre-ignition to super-knock: hotspot-induced deflagration to detonation. Fuel 2015;144:222–7.
[18] Liu W, et al. Simultaneous lateral- and end-view visualization of the auto-ignition of primary reference fuels in a rapid compression machine. Combust Flame 2023; 256:112957.
[19] Tang Q, et al. Study of engine knocking combustion using simultaneous high-speed shadowgraph and natural flame luminosity imaging. Appl Therm Eng 2023;235: 121440.
[20] Shi H, et al. Optical diagnostics and multi-point pressure sensing on the knocking combustion with multiple spark ignition. Combust Flame 2022;236:111802.
[21] Tanoue K. Effect of autoignition characteristic of fuels on knocking properties. Int J Engine Res 2016;17(6):666–76.
[22] Terashima H, et al. Mechanisms of strong pressure wave generation in end-gas autoignition during knocking combustion. Combust Flame 2015;162:1944–56.
[23] Robert A, et al. LES study of deflagration to detonation mechanisms in downsized spark ignition engine. Combust Flame 2015;162:2788–807.
[24] Terashima H, et al. Origin and reactivity of hot-spots in end-gas autoignition with effects of negative temperature coefficients: relevance to pressure wave developments. Combust Flame 2017;184:324–34.
[25] Szwaja S, et al. Dual nature of hydrogen combustion knock. Int J Hydrogen Energy 2013;38:12489–96.
[26] Manzoor MU, et al. "Capturing different modes of hydrogen combustion in a spark-ignition engine using numerical simulations". Fuel 2024;375:132343.
[27] Wang L, et al. Defining and predicting end-gas autoignition boundaries for knock control in hydrogen engines. Int J Hydrogen Energy 2026;229:154687.
[28] Li Y, et al. Numerical investigation on combustion and knock formation mechanism of hydrogen direct injection engine. Fuel 2022;316:123302.
[29] Lou D, et al. Investigation of impacts of hydrogen injection and spark strategy on knock in hydrogen engine. Int J Hydrogen Energy 2024;82:1252–2362.
[30] Lou D, et al. Insight into the effects of equivalence ratio: a multivariate analysis of combustion phasing, performance and knock in a Hydrogen-fueled engine. Int J Hydrogen Energy 2026;216:153946.
[31] Manzoor MU, et al. Normal and knocking combustion of hydrogen: a numerical study. Fuel 2023;344:128093.
[32] Pan J, et al. Interactions of flame propagation, auto-ignition and pressure wave during knocking combustion. Combust Flame 2016;164:319–28.
[33] Zeldovich YAB. Regime classification of an exothermic reaction with nonuniform initial conditions. Combust Flame 1980;39:211–4.
[34] D. Bradley et al., "Amplified pressure waves during autoignition: relevance to CAI engines", SAE 2002-01-2868.
[35] Gu XJ, et al. Modes of reaction front propagation from hot spots. Combust Flame 2003;133:63–74.
[36] Robert A, et al. Numerical study of auto-ignition propagation modes in toluene reference fuel-air mixtures: toward a better understanding of abnormal combustion in spark-ignition engines. Int J Engine Res 2019;20(7):734–45.
[37] Azimov U, et al. Premixed mixture ignition in the end-gas region (PREMIER) combustion in a natural gas dual-fuel engine: operating range and exhaust emissions. Int J Engine Res 2011;12(5):484–97.
[38] Imamoto T, et al. PREMIER combustion characteristics of a pilot fuel-ignited dual-fuel biogas engine with consideration of cycle-to-cycle variations. Fuel 2022;314: 123049.
[39] Mesa CK, et al. Combustion characteristics of a pilot fuel-ignited dual-fuel hydrogen gas engine with nitrogen dilution. J Energy Inst 2025;123:102296.
[40] Kawahara N. Differences between PREMIER combustion in a natural gas spark-ignition engine and knocking with pressure oscillations. Proc Combust Inst 2019; 37:4983–91.
[41] Nirendra M, et al. Injection-timing-induced end-gas autoignition and knock control in a natural gas/diesel dual-fuel engine under lean operation. Int J Engine Res 2026. https://doi.org/10.1177/14680874261461671.
[42] Kawahara N, et al. Visualization of auto-ignition and pressure wave during knocking in a hydrogen spark-ignition engine. Int J Hydrogen Energy 2009;34: 3156–63.
[43] Gaydon AG. The spectroscopy of flames. London: Chapman and Hall; 1957.
[44] Schefer RW, et al. Visible emission of hydrogen flames. Combust Flame 2009;156: 1234–41.
[45] Ferguson CR, et al. Internal combustion engines applied thermosciences. Third Edition; 2016.
[46] Berenjestanaki AV, et al. Performance, emissions and end-gas autoignition characteristics of PREMIER combustion in a pilot fuel-ignited dual-fuel biogas engine with various CO_2 ratios. Fuel 2021;286:119330.
[47] M. Katsumata et al., "Behavior of shock wave and pressure wave of SI knocking with super rapid compression machine", SAE 2011-01-1875.
[48] Otsu N. A threshold selection method from gray-level histograms. IEEE Trans Syst Man Cybern 1979;9(1):62–6. N.
[49] Kawahara et al., "Visualization of autoignited kernel and propagation of pressure wave during knocking combustion in a hydrogen spark-ignition engine", SAE 2009-01-1773.
[50] ANSYS CHEMKIN-Pro, Release 2025 R1, ANSYS Inc., Canonsburg, PA, USA.
[51] Miyoshi A. *KUCRS software library*, revision *yyyymmdd*. available from: the author. See the web: http://akrmys.com/KUCRS/forupdateinformation.
[52] Lutz AE, et al. Dynamic effects of autoignition centers for hydrogen and $C_{1,2}$-hydrocarbon fuels. Twenty-second symposium (international) on combustion. The Combustion Institute; 1988. p. 1683–93.
[53] G.T. Kalghatgi et al, "Pre-ignition and 'super-knock' in turbo-charged spark-ignition engines", Int J Engine Res 13(4) 399-414.
[54] Bradley D. Autoignitions and detonations in engines and ducts. Phil Trans R Soc A 2012;370:689–714.